MIT Libraries | DSpace@MIT

MIT Open Access Articles

Thermospheric poleward wind surge at midlatitudes during great storm intervals

Massachusetts Institute of Technology

1 **Thermospheric Poleward Wind Surge at Mid-Latitudes During Great**

2 **Storm Intervals**

3

4 Shun-Rong Zhang[1,*], Philip J. Erickson[1], John C. Foster[1], John M. Holt[1], Anthea J.

5 Coster[1], Jonathan J. Makela[2], John Noto[3], John W. Meriwether[4], Brian J. Harding[2],

6 Juanita Riccobono[3] and Robert B. Kerr[3]

7

8 *1 MIT Haystack Observatory, Westford, MA, USA*

9 2 Department of Electrical and Computer Engineering, *University of Illinois at*

10   *Urbana-Champaign, Urbana, Illinois, USA*

11 3 *Scientific Solution, Inc., Chelmsford, MA, USA*

12 *4 Department of Physics and Astronomy, Clemson University, Clemson, SC, USA*

13
14   *** Correspondence:**

15   Dr. Shunrong Zhang (shunrong@haystack.mit.edu)

16   MIT Haystack Observatory

17   Off Route 40

18   Westford, MA 01886

19   USA

20

21 **Key points**

22 1. Pre-midnight poleward wind surge at 100m/s, preceded by 300m/s westward

23   winds

24 2. No equatorward wind surge developed throughout the night

25 2. Disturbance wind driven by Subauroral Polarization Streams and Coriolis force

26

27   **Abstract**

28

29   We report a significant poleward surge in thermospheric winds at subauroral and mid

30   latitudes following the 17-18 March 2015 great geomagnetic storm. This pre-midnight

31   surge is preceded by strong westward winds. These disturbances were observed over

32   three sites with geodetic latitudes 35-42°N in the American sector by Fabry-Perot

33   interferometers at 630-nm wavelength. Prior to the wind disturbances, subauroral

34   polarization streams (SAPS), were measured by the Millstone Hill incoherent scatter

35   radar between 20-02 UT. We identify the observed neutral wind variations as driven by

36   SAPS, through a scenario where strong ion flows cause a westward neutral wind,

37   subsequently establishing a poleward wind surge due to the poleward Coriolis force on

38   that westward wind. These regional disturbances appear to have prevented the well-

39   known storm time equatorward wind surge from propagating into low latitudes, with the

40   consequence that the classic disturbance dynamo mechanism failed to occur.

41

1. **Introduction**

An equatorward surge of thermospheric meridional neutral wind at mid-latitudes is a common dynamic feature of Earth's neutral atmosphere during geomagnetic storms. Numerous studies have shown in detail how storm time momentum and energetic inputs perturb the high-latitude ionosphere and thermosphere, with subsequent equatorward propagation of disturbances [see reviews, Matuura, 1972; Prolss, 1995; Buonsanto, 1999; Mendillo, 2006]. In particular, the storm time equatorward wind generated by impulsive polar latitude heating processes can be very strong at night (1) when disturbance effects add to the quiet time equatorward neutral circulation [Rishbeth, 1989], and (2) when high-latitude convection is enhanced and expanded equatorward causing a significant anti-sunward ion flow [e.g., Straus and Schulz, 1976]. Due to the Coriolis force, the equatorward wind surge can subsequently drive a westward neutral wind disturbance as it reaches mid- and low-latitudes. These wind disturbances are at the heart of the important ionospheric dynamo effect [Blanc and Richmond, 1980; Fuller-Rowell et al., 2002] and equatorward wind surges have been the subject of prior studies [e.g., Meriwether, 2008].

However, equatorward wind surges do not necessarily occur during every storm. In fact, the disturbance wind undergoes substantial variability with local time, season and solar activity for a given location. Fejer et al. [2002] showed that at Millstone Hill (MH, 42.6^{o}N, 71.5^{o}W; geodetic), storm time winds sometimes turn poleward following a midnight or post-midnight equatorward surge (in particular for solar minimum). The pre-midnight meridional wind disturbance, however, is generally weak and equatorward, occasionally with a very small and brief poleward turning. The poleward wind surge can be also seen as traveling atmosphere disturbances (TADs) from the opposite hemisphere [e.g., Shiokawa et al., 2003].

71   This paper reports a fundamentally different neutral wind scenario observed over three

72   sites at mid and subauroral latitudes during the 17-18 March 2015 great storm. During

73   this event, the pre-midnight meridional wind turns poleward and remains in this direction

74   for a few hours. Using a joint analysis of incoherent scatter radar (ISR) and Fabry-Perot

75   interferometer (FPI) observations along with first-principles model simulations, we show

76   in this paper that the anomalous poleward wind originated from the Subauroral

77   Polarization Stream (SAPS) [Foster and Vo, 2002], a characteristic storm time

78   magnetosphere-ionosphere coupling feature within a relatively narrow region of low

79   ionospheric conductivity between the auroral precipitation zone and the plasmasphere

80   boundary layer [Carpenter and Lemaire, 2004]. Strong SAPS flows overlap the

81   plasmasphere edge and provide a significant convective force moving plasma against

82   corotation from the dusk sector toward the noontime cusp in storm enhanced density

83   (SED) features [Foster, 1993; Kelly et al., 2004], also known as the dusk effect

84   [Mendillo, 2006]. Sunward ion flow in the late afternoon sector (with a poleward

85   component) also causes SED plasma to drift upwards at subauroral latitudes into regions

86   where recombination rates are significantly reduced, leading to high electron density

87   values [Heelis, 2008]. Strong plasma flow has reportedly produced enhanced neutral

88   westward winds [e.g., Wang H. et al., 2011] due to strong ion drag effects. TIEGCM

89   simulations [Wang W. et al., 2012] confirm expected ion drag effects in the

90   thermospheric temperature and zonal winds on a global scale.

91

92   **2. Observations and Analysis Procedure**

93

94   Following the arrival of a Coronal Mass Ejection (CME) and under the influence of high-

95   speed solar wind streams, severe/great geomagnetic disturbances occurred for an

96   extended period starting on 17 March 2015 (Figures 1a-b). Interplanetary Magnetic Field

97   (IMF) northward component Bz hourly values in Geocentric Solar Magnetospheric

98   (GSM) coordinates fell to -14 nT between 05 - 08 UT, and then underwent a 12-hour

99   long sustained negative disturbance of ~ -17 nT between 12 - 24 UT on the 17th. During

100   this time, the hourly Dst index dropped to a minimum of -227 nT at 23 UT. The 3-hourly

101   Kp value jumped to 5- with the initial Bz negative excursion, reaching between 8- and 7+

102   during the large and long-lasting drop in Bz.

103

104   These geospace disturbances caused a series of significant changes in earth's ionosphere

105   and thermosphere. Figure 1(c) plots TEC disturbances, as derived from global GPS

106   ground receiver data by MIT Haystack Observatory MAPGPS software [Rideout and

107   Coster, 2006]. The TEC disturbances are defined here as the mean TEC value in each 3°

108   latitude bin over 30-50° N geodetic latitudes over the MH longitude (70-80° W) after

109   undisturbed background TEC has been subtracted using a monthly-average based

110   empirical model [Chen et al., 2014]. An initial positive disturbance of more than 50% is

111   seen poleward of MH following the first Bz equatorward turning. A narrow enhancement

112   zone at 18 UT is visible, and subsequent enhancements extended and expanded from MH

113   latitudes at 21 UT to lower latitudes at 23 UT. Subsequent sharp decreases of ~ 50%

114   expanded from 50° N at 20 UT to 37° N within 4 hours.

115

116   This equatorward moving density reduction zone eventually remained at 38-42°N

117   between 24-05 UT. It is during these pre-midnight hours, and within the midlatitude

118   trough, that both SAPS and neutral wind disturbances were observed (Section 3). The

119   presence of a SAPS flow channel is further evidenced by MH ISR observations (Section

120   3). The ~50% TEC enhancement seen equatorward of the trough is a typical SED

121   characteristic, and is a result of plasmaspheric erosion associated with SAPS. Later

122   sections will present these radar observations and will discuss the connection between

123   SAPS and neutral wind disturbances.

124

125   During this storm, an international observation campaign along the meridian circle of

126   60°W/120°E longitude was conducted. In particular, excellent ionospheric plasma

127   information from ISRs and neutral atmosphere information from FPIs is available in the

128   western hemisphere, along with other observational facilities supported by the Chinese

129   Meridian Project [Wang, 2010] and other institutions in the eastern hemisphere.

130

131   At mid-latitudes, the MH ISR operated in an experimental sequence using both zenith

132   and steerable antennas providing local, regional, and wide coverage. The wide coverage

133   is provided by low (6°) elevation radar scans from north to west of Millstone Hill while

134   regional coverage uses 45° elevation positions in north and west directions combined

135   with zenith observations. Combining line-of-sight (LOS) ion velocities in these multiple

136   directions allows derivation of key components of F-region ion velocity perpendicular to

137   the magnetic field: VperE, eastward perpendicular to magnetic field **B**, and VperN,

138   poleward perpendicular to **B**. VperE is determined to the northwest of MH at ~(47^oN,

139   89^oW) from the west-looking data using azimuths in the (-100, -45) degree range. VperN

140   is determined for MH north at ~(53^oN, 75^oW) from low elevation north-looking data such

141   that LOS is nearly perpendicular to the magnetic field. These observations provide

142   evidence of SAPS.

143

144   FPIs observing the thermospheric 630.0-nm emission arising from dissociative

145   recombination of O_2^+ provide LOS measurements of neutral winds at typical emission

146   heights of ~250 km altitude. Data from three sites in North America were used in this

147   study. At MH, the emission is detected from look directions in the north, east, south,

148   west (all with 45° elevation) and zenith. The other two FPI redline sites are from the

149   North American Thermosphere-Ionosphere Observing Network (NATION) [Makela et

150   al., 2014]: Urbana Atmospheric Observatory (UAO, 40.13^oN, 88.20^oW) and Pisgah

151   Astronomical Research Institute (PAR, 35.2^oN, 82.85^oW) [Makela et al., 2011]. They

152   have similar look angles to MH, with the addition of a pointing direction upward along **B.**

153   A typical observational cycle takes 12 min for NATION sites (15 min for MH), and data

154   are analyzed using the methodology described in Harding et al. [2014]. During the 17-18

155   March night, the skies over PAR became partly cloudy after 0630 UT on 18 March, and

156   the skies over UAO became partly cloudy after ~03 UT, but these facts do not

157   significantly affect results for the key period addressed by this work. Additionally, the

158   apparent vertical wind conditions described in Makela et al. [2014] did not seem to occur

159   during the observations reported here, making the small vertical wind assumption,

160   typically used when analyzing FPI observations, valid. To estimate the neutral wind

161   vector based on LOS FPI observations, we follow a procedure where the vector velocity

162   is determined through a least-squared fit algorithm using the combined LOS data from all

163   directions within 36 min (45 min for MH), weighted by the LOS errors. Standard

164   deviations on the resulting vector neutral winds are also given.

165

166   **3. Superstorm Thermospheric and Ionospheric Response**

167

168   FPI observations during the evening of 17-18 March began just after the main phase of

169   the storm at the time of maximum ring current intensity / minimum Dst value, as Bz

170   started to return to positive values. At MH (Figure 2), a strong westward zonal wind of

171   300 m/s was already established, at a 350 m/s offset from its monthly mean in the

172   eastward direction. The strong westward wind then weakened after 02 UT, and stayed at

173   200 m/s for 2 hours. During the next 3 hours, the westward zonal wind eventually

174   returned to its monthly mean and the disturbance vanished after local midnight. The

175   meridional wind component started slightly equatorward then subsequently became

176   significantly poleward, eventually reaching 100 m/s at 0230-0300 UT (~22 LT). The

177   poleward wind surge was significant between 2030 and 2230 LT, primarily before

178   midnight. Following this period, the meridional wind returned to its monthly mean value

179   and remained in line with monthly averages without any further equatorward or poleward

180   surges.

181

182   FPI observations at UAO at latitudes comparable to MH show very similar features. In

183   particular, a strong westward zonal wind lasting ~2 hours was followed by a 2-hour long

184   poleward meridional wind surge, reaching 100 m/s at 0230 UT. The PAR FPI station is

185   5° to the south of UAO and MH, and the poleward wind abatement, reaching 100 m/s at

186   0300 UT, is preceded by a strong westward enhancement for ~2 hours. The westward

187   wind enhancement is not as strong at PAR as at the other two higher latitude sites.

188

189   Prior to the occurrence of these neutral wind disturbances, strong ionospheric

190   disturbances were observed such as the midlatitude trough, SEDs, and associated SAPS

191 flows. Figure 3 shows VperE (perpendicular eastward, a) in the west and VperN
192 (perpendicular northward, b) in the north of MH on 17-18 March as well as later on 19
193 March, where observations for the latter half of the 18th and first half of the 19th can be
194 considered representative of normal ionospheric conditions due to relatively low
195 magnetic activity.

196

197 The magnetically zonal ion drift, VperE, turned westward at 20 UT. In the next 5 hours,
198 this westward drift remained very strong at 500-750 m/s. We identified the high-speed
199 ion flow as SAPS since it is situated near the low density (midlatitude trough) region as
200 evidenced in TEC (Figure 1c) and also in the ISR measured electron content IEC (Figure
201 3d). SAPS features are also associated with SED passage over MH, prior to the SAPS
202 local onset, as shown in the TEC plume equatorward of the trough (Figure 1c) and in the
203 IEC peak at 20UT (Figure 3c). Since the ion speed is faster than the speed of the neutrals,
204 SAPS will accordingly drive the neutrals in the same direction. MH and UAO zonal
205 winds in Figure 2 are shown in Figure 3(e) to highlight this neutral and ion velocity
206 connection. Even though the exact onset time of the westward neutral wind
207 enhancements are unknown due to lack of data prior to 00 UT, the enhancements
208 weakened around 02-03UT when the large westward ion drift disappeared. The largest
209 westward wind surge (~400 m/s) is at UAO where the TEC drop appears the most
210 significant, and therefore SAPS peak velocities are expected to be the strongest.

211

212 The neutral wind disturbance, and in particular the poleward surge, can be seen in the
213 upward ion drift Vz at 250 km (Figure 3c). Between 01-05 UT on 18 March when
214 electric fields are quiet, Vz is more negative (downward) compared to the reference,
215 suggesting that the poleward wind surge makes a significant contribution.

216

217 The radar data shows also a strong poleward ion drift VperN at ~55°N, in particular,
218 between 20-23 UT. Combining these northward and westward components, it is likely
219 that the sunward drift is a significant factor in producing the large observed SED plumes
220 in TEC and IEC data.

221

4. Simulation of Wind Effects

222

223

4.1 March 17th Event Summary

The observations described in Section 3 are consistent with the following timeline of ionosphere and thermosphere processes during the 17-18 March superstorm: (1) At ~21 UT on 17 March, SED plumes are present, observed as TEC and IEC enhancements, along with onset of strong SAPS westward ion drift of >500 m/s peaking in the midlatitude trough of the American sector; (2) Starting at about 22 UT, a strong westward neutral wind appears (with greater amplitude in the trough region of ~40 - 42°N latitude as compared to 35°N) and lasts for 4 hours until 02 UT on 18 March. After 02 UT, the zonal wind amplitude decreased dramatically (at higher latitudes) or gradually (at lower latitudes); and (3) At 03 UT, a poleward wind surge of ~100 m/s occurs. We posit that the chain of events from (1) to (3) are a result of ion-neutral coupling and thermospheric dynamical processes. In particular, the westward neutral wind characteristics described in (2) are attributable to the well-known ion drag effect following the onset of SAPS described in (1). Our proposition is further indicated by the observation that westward neutral wind anomalies disappeared when SAPS forcing disappeared, with the effects strongest in the area of the deepest midlatitude trough. Subsequently, the poleward wind surge described in (3) is produced following strong westward winds as described in (2) because of the poleward Coriolis force arising from significant westward wind amplitudes.

243

4.2 Simulated F-region westward ion drift effects

To explore the validity of this scenario, an ion-neutral coupling simulation was conducted with parameters characteristic of mid-latitudes near Millstone Hill. This relatively simple simulation was designed to study the basic proposed mechanism and its general features, rather than reproducing all observational details. The numerical experiment utilizes a local ionosphere-thermosphere wind coupling model. The ionospheric model [Zhang and Huang, 1995; Zhang et al., 2003] solves the equation of mass continuity for multiple ions

251   and the equation of momentum for O^+. Ionospheric temperatures are set to the empirical

252   ISR Ionospheric Model (ISRIM) for MH [Zhang et al., 2005; 2007b]. The non-

253   disturbance electric field is specified by the local electric fields derived from the

254   statistical Millstone Hill – Sondrestrom convection model [Zhang et al., 2007a]. Neutral

255   densities and temperatures are specified by the NRL-MSIS model [Picone et al., 2002].

256   The neutral wind calculation is based on solving the momentum equation for the neutral

257   gas where pressure gradients are derived from the NRL-MSIS model. A resolution of 2-

258   min in time and 2-km in altitude is used. Other details of the simulation are described

259

260   A baseline / reference run for medium solar activity levels at equinox, corresponding to

261   17 March 2015 conditions, was performed without imposing the observed westward ion

262   drift. A second run included a 500 m/s westward ion drift imposed during 18-21 LT (23-

263   02 UT). This 500 m/s value represents a modest enhancement in zonal ion velocity

264   compared to the ISR measured SAPS speed on 17 March (cf. Section 3). The top panel of

265   Figure 4 plots the calculated model profiles of electron density and neutral winds at 1930

266   LT, 1.5 hours into the strong westward ion drift injection event. The middle panel shows

267   differential changes in calculated poleward and eastward winds relative to the reference

268   run. The differential results clearly show a build-up of westward winds within one hour

269   following SAPS turn-on, saturating at 300 m/s at ~1930 LT. This ~200 m/s difference in

270   flow speeds between ions and neutrals created frictional heating leading to neutral

271   temperature increases (not shown). The poleward wind showed a different behavior,

272   gradually increasing in speed but at slower rates compared to westward wind increases.

273   In particular, northern wind differential values peaked at 130 m/s at ~2130 LT, with a

274   delay of ~2 hours following westward neutral flow saturation and ~3.5 hours following

275   SAPS initiation. These time constants are governed by background thermospheric density

276   and temperature, which undergo substantial storm time changes (and therefore the real

277   response times can be quite different from simulated results.) In the simulation, the

278   Coriolis force is the only mechanism that connects the zonal and meridional winds, so the

279   key finding is that poleward wind buildup is caused by Coriolis force effects in the north

280 direction because of westward neutral motion, with the characteristic time delay in storm

281 time variations between the two components as another sign of Coriolis forcing.

282

283 The third panel of Figure 4 plots ionospheric electron density differential response to

284 strong westward ion drift. The peak height, hmF2, dropped by ~55 km during the period

285 of significant poleward wind, and NmF2 dropped by ~80% after the westward ion drift

286 ceased. In this numerical experiment, the electron density reduction is achieved by the

287 induced poleward winds only, but an increase in the ion recombination rate caused by

288 frictional heating can further reduce the F-region electron density [Schunk et al., 1975].

289

290 **5. Discussion**

291

292 Reproducing all observational details with the numerical experiment in Section 4 is not

293 possible because of the simulation's simplified treatment of ion and neutral temperatures

294 and neutral densities, which in reality are likely subject to large offsets from the empirical

295 model specifications used in this storm study. In particular, we have ignored the potential

296 presence of meridional pressure gradients to the north of MH, produced by the same

297 auroral heating processes that likely would generate an equatorward wind surge. The

298 simulated poleward surge produced by Coriolis force action is smooth and gradual in

299 time.   This is quite similar to FPI observations at the lower latitude site, PAR.   By

300 contrast, at the higher latitude of MH the observed poleward surge grows faster than in

301 the simulation. A more precise neutral response simulation would require a better

302 specification of storm time neutral density and temperature.   In general, more

303 sophisticated modeling is needed to put the regional observations into correct global

304 context and to better explain observational features.   However, the initial simplified

305 simulation presented here is sufficient to demonstrate that ion-neutral coupling and

306 Coriolis force effects are likely to play fundamental roles in observed wind dynamics.

307

308 Coriolis force effects on westward neutral wind amplitude were noted in an earlier

309 numerical experiment by Forbes and Roble [1990]. Hagan and Sipler [1991] also report a

310 similar set of observed ionospheric and thermospheric storm time effects with smaller

311 westward wind and minor meridional wind abatement during the 7-10 March 1989 storm

312 at MH. They pointed out that westward winds caused diminishment of equatorward wind

313 surges due to Coriolis forces. Hernandez et al. [1982] reported a converging wind system

314 measured by the FPI over Fritz Park (39.9°N, 105.5°W) during two major storms where

315 similar ion-neutral interaction was speculated for the south of the site. It appears that

316 large westward winds, the poleward turning of the wind, and low electron densities are all

317 potential consequences of ion-neutral coupling in some large storm events such as

318 presented here.

319

320 During large geospace storm intervals, TADs are often observed, and in fact poleward

321 winds observed at lower mid-latitudes in Asia were explained as resulting from TAD

322 passage with a disturbance source region in the south [e.g., Shiokawa et al., 2003]. This

323 study, however, does not show obvious signs of propagating waves as in the TAD

324 scenario. In particular, the poleward wind surge and westward wind enhancement appear

325 stronger at subauroral latitudes than at lower latitudes, counter to expectations of a TAD

326 mechanism to the south generating atmospheric waves. TADs from sources to the north

327 would cause equatorward wind perturbations, not poleward as observed.

328

329 **6. Summary and conclusion**

330

331 Strong geospace disturbances during the 17-18 March 2015 superstorm produced intense

332 electric fields at subauroral and mid-latitudes. SED plumes shown in TEC and ISR

333 electron content enhancements over the northeast US are present prior to 21 UT before

334 passage of the midlatitude trough. A strong westward ion drift, identified as SAPS, then

335 developed during 21-02 UT, as observed by the Millstone Hill ISR. This drift, drove

336 neutral particles westward, causing a strong westward neutral wind (~300 m/s) observed

337 by multiple FPIs between 35-42°N latitudes in the American sector. Later in the event, a

338 poleward neutral wind response occurred due to Coriolis force effects on the westward

339 neutral wind. The poleward wind, directly observed by the FPIs, eventually reached 100

340　　m/s amplitude in a few hours following the onset of SAPS. A simplified numerical model

341　　with coupling of ionospheric density and thermospheric neutral winds is able to

342　　demonstrate response characteristics of this mechanism that reasonably match general

343　　observational features. We conclude that unusual neutral wind disturbances in both zonal

344　　and meridional directions have their ultimate source in the SAPS electric field which

345　　generates substantial ion flows and leads to strong ion-neutral interaction.

346

347　　We point out that the observed pre-midnight storm time surge in the poleward wind

348　　implies a regional circulation background that may prevent propagation of the auroral

349　　heating produced equatorward wind surge to lower latitudes, and would therefore prevent

350　　development of the classic disturbance dynamo. If correct, this mechanism may

351　　substantially influence the storm time low latitude and equatorial electrodynamic

352　　response in some cases [Fejer and Scherliess, 1995; Maruyama et al., 2005; Lu et al.,

353　　2012]. Thus, further investigation is needed to characterize westward ion drifts at

354　　subauroral latitudes, including SAPS, as a significant driving factor, and to understand

355　　more fully how the SAPS driven neutral wind disturbances are affected by storm-time

356　　ionosphere and thermosphere conditions.

357

12

389
390
391

392

393

394 **References**

395

396 Blanc, M., and A. D. Richmond (1980), The ionospheric disturbance dynamo, J.
397 Geophys. Res., 85, 1669–1686.

398

399 Buonsanto, M. J. (1999), Ionospheric storms—A review, Space Sci. Rev., 88, 563–601.

400

401 Buonsanto, M. J., Foster, J. C., Galasso, A. D., Sipler, D. P., Holt, J. M. (1990) Neutral
402 Winds and Thermosphere/Ionosphere Coupling and Energetics During the Geomagnetic
403 Disturbances of March 6–10, 1989. J. Geophys. Res. 95: pp. 21033-21050

404

405 Carpenter, D. and J. Lemaire (2004), The plasmasphere boundary layer, Ann. Geophys.
406 22, 4291–4298.

407

408 Chen, Z., S.-R. Zhang, A. J. Coster, and G. Fang (2015), EOF analysis and modeling of
409 GPS TEC climatology over North America, J. Geophys. Res. Space Physics, 120,
410 doi:10.1002/2014JA020837.

411

412 Fejer, B. G. (2002), Climatology and storm time dependence of nighttime thermospheric
413 neutral winds over Millstone Hill, J. Geophys. Res., 107(A5), 1052,
414 doi:10.1029/2001JA000300.

415

416 Fejer, B. G., and L. Scherliess (1995), Time dependent response of equatorial ionospheric
417 electric fields to magnetospheric disturbances, Geophys. Res. Lett., 22(7), 851–854,
418 doi:10.1029/95GL00390.

419

420 Foster, J. C. (1993), Storm time plasma transport at middle and high latitudes, *J.
421 Geophys. Res.*, 98, 1675–1690.

422

423 Foster, J. C., and H. B. Vo (2002), Average Characteristics and Activity Dependence of
424 the Subauroral Polarization Stream, *J. Geophys. Res.*, 107(A12),1475, doi:
425 10.1029/2002JA009409.

426

427 Forbes, J. M., and R. G. Roble (1990), Thermosphere-ionosphere coupling: An
428 experiment in interactive modeling, J. Geophys. Res., 95(A1), 201,
429 doi:10.1029/JA095iA01p00201.

430

431 Fuller-Rowell, T. J., G. H. Millward, A. D. Richmond, and M. V. Codrescu (2002),
432 Storm-time changes in the upper atmosphere at low latitudes, J. Atmos. Sol. Terr. Phys.,
433 64, 1383.

434

435 Hagan, M. E., and D. P. Sipler (1991), Combined incoherent scatter radar and Fabry-
436 Perot interferometer measurements of frictional heating effects over Millstone Hill during
437 March 7–10, 1989, J. Geophys. Res., 96(A1), 289, doi:10.1029/90JA02250.
438

439 Harding, B. J., T. W. Gehrels, and J. J. Makela (2014), Nonlinear regression
440 method for estimating neutral wind and temperature from Fabry–Perot
441 interferometer data, Appl. Opt., 53(4), 666.

442 Heelis, R. A. (2008) Low- and Middle-Latitude Ionospheric Dynamics Associated with

443 Magnetic Storms, in Midlatitude Ionospheric Dynamics and Disturbances (eds P. M.

444 Kintner, A. J. Coster, T. Fuller-Rowell, A. J. Mannucci, M. Mendillo and R. Heelis),

445 American Geophysical Union, Washington, D. C.. doi: 10.1029/181GM06

446 Hernandez, G., R. G. Roble, E. C. Ridley, and J. H. Allen (1982), Thermospheric
447 response observed over Fritz Peak, Colorado, during two large geomagnetic storms near
448 Solar Cycle Maximum, *J. Geophys. Res.*, *87*(A11), 9181-9192, doi:10.1029/JA087.
449
450
451 Lu, G., L. Goncharenko, M. J. Nicolls, A. Maute, A. Coster, and L. J. Paxton (2012),
452 Ionospheric and thermospheric variations associated with prompt penetration electric
453 fields, J. Geophys. Res., 117, A08312, doi:10.1029/2012JA017769.
454
455 Makela, J. J., J. W. Meriwether, Y. Huang, and P. J. Sherwood (2011), Simulation and
456 analysis of a multi-order imaging Fabry–Perot interferometer for the study of
457 thermospheric winds and temperatures, Appl. Opt., 50, 4403-4416.
458
459 Makela, J. J., et al. (2014), Storm time response of the midlatitude thermosphere:
460 Observations from a network of Fabry-Perot interferometers, J. Geophys. Res. Space
461 Physics, 119, 6758–6773, doi:10.1002/2014JA019832.
462
463 Matuura, N. (1972), Theoretical models of ionospheric storms, Space Sci. Rev., 13, 124–
464 189.
465
466 Mendillo, M. (2006), Storms in the ionosphere: Patterns and processes for total electron
467 content, Rev. Geophys., 44, RG4001, doi:10.1029/2005RG000193.
468
469 Maruyama, N., A. D. Richmond, T. J. Fuller-Rowell, M. V. Codrescu, S. Sazykin, F. R.
470 Toffoletto, R. W. Spiro, and G. H. Millward (2005), Interaction between direct
471 penetration and disturbance dynamo electric fields in the storm-time equatorial
472 ionosphere, Geophys. Res. Lett., 32, L17105, doi:10.1029/2005GL023763.
473
474 Picone, J. M., A. E. Hedin, D. P. Drob, and A. C. Aikin, NRLMSISE-00 empirical model
475 of the atmosphere: Statistical comparisons and scientific issues, J. Geophys. Res.,
476 107(A12), 1468, doi:10.1029/2002JA009430, 2002.

477

478 Prölss, G. W. (1995), Ionospheric F-region storms, in Handbook of Atmospheric
479 Electrodynamics, vol. 2, edited by H. Volland, chap. 8, pp. 195–248, CRC Press, Boca
480 Raton, Fla.

481

482 Rideout, W., and A. Coster (2006), Automated GPS processing for global total electron
483 content data, GPS Solut., 10, 219–228, doi:10.1007/s10291-006-0029-5.

484

485 Rishbeth, H. (1998), How the thermospheric circulation affects the ionospheric F2-layer,
486 J. Atmo. Sol.-Terr. Phys., 60(14), 1385–1402.

487

488 Schunk, R. W., W. J. Raitt, and P. M. Banks (1975), Effect of electric fields on the
489 daytime high-latitude E and F regions, J. Geophys. Res., 80, 3121.

490

491 Shiokawa, K., et al. (2003), Thermospheric wind during a storm-time large-scale
492 traveling ionospheric disturbance, J. Geophys. Res., 108, 1423,
493 doi:10.1029/2003JA010001, A12.

494

495 Straus, J.M., Schulz, M. (1976), Magnetospheric Convection and Upper Atmospheric
496 Dynamics'. J. Geophys. Res. 81, 5822-5832.

497

498 Wang, C. (2010), New Chains of Space Weather Monitoring Stations in China. Space
499 Weather, 8: n/a. doi: 10.1029/2010SW000603

500

501 Wang, W., E. R. Talaat, A. G. Burns, B. Emery, S. Hsieh, J. Lei, and J. Xu (2012),
502 Thermosphere and ionosphere response to subauroral polarization streams (SAPS):
503 Model simulations, J. Geophys. Res., 117, A07301, doi:10.1029/2012JA017656.

504

505 Wang, H., H. Lühr, K. Häusler, and P. Ritter (2011), Effect of subauroral polarization
506 streams on the thermosphere: A statistical study, J. Geophys. Res., 116, A03312,
507 doi:10.1029/2010JA016236.

508

509 Zhang S.-R. and X.-Y. Huang (1995), A Numerical Study of Ionospheric Profiles for
510 Mid-Latitudes, Ann Geophysicae, 13, 551-557.

511

512 Zhang, S.-R. W. L. Oliver, J. M. Holt, and S. Fukao (2003), Ionospheric data
513 assimilation: Comparison of extracted parameters using full density profiles and key
514 parameters, J. Geophys. Res. 108, 10.1029/2002JA009521.

515

516 Zhang, S.-R., J. M. Holt, A. P. van Eyken, M. McCready, C. Amory-Mazaudier, S.
517 Fukao, and M. Sulzer (2005), Ionospheric local model and climatology from long-term
518 databases of multiple incoherent scatter radars, Geophys. Res. Lett., 32, L20102,
519 doi:10.1029/2005GL023603

520

521   Zhang, S.-R. and J. M. Holt (2007a), Ionospheric Climatology and Variability from
522   Long-term and Multiple Incoherent Scatter Radar Observations: Climatology in Eastern
523   American Sector, J. Geophys. Res., 12, A06328, doi:10.1029/2006JA012206
524
525   Zhang, S.-R., J. M. Holt, and M. McReady (2007b), High latitude convection model
526   based on long-term incoherent scatter radar observations in North America, J. Atmos.
527   Sol.-Terr. Phys., 69, 1273-1291, doi:10.1016/j.jastp.2006.08.017
528
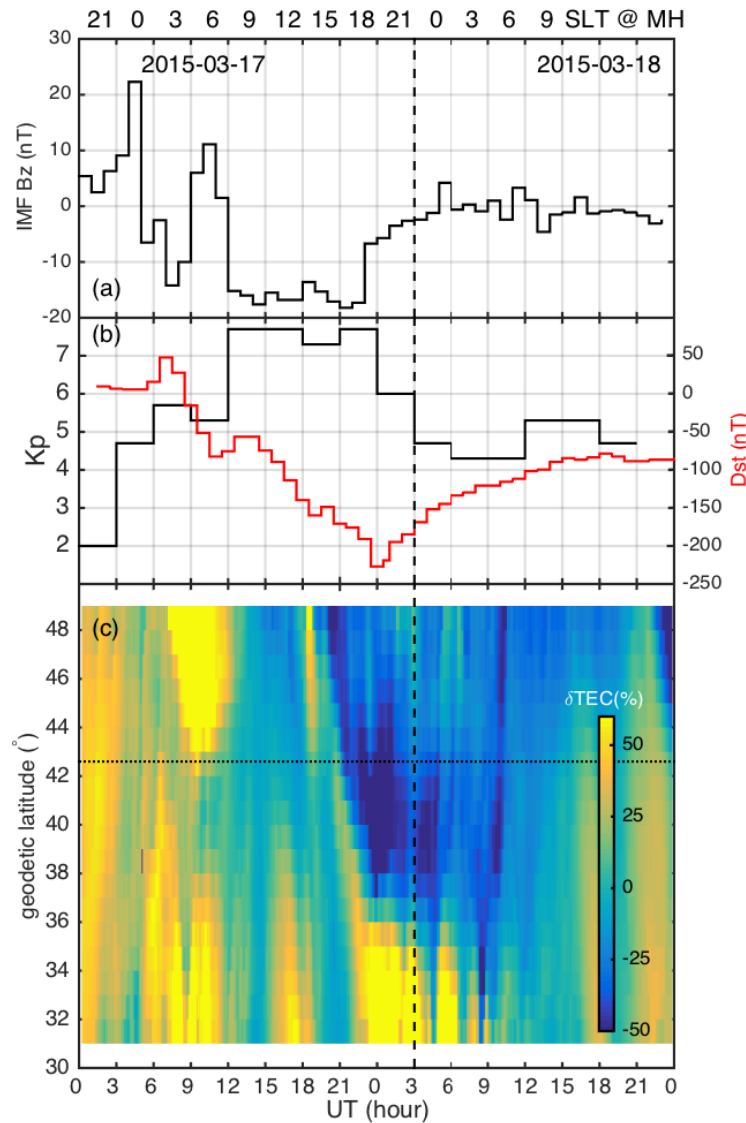
Figure 1. Solar geophysical conditions during March 17-18, 2015: hourly IMF Bz (a), 3-hourly Kp and hourly Dst (b), and GPS TEC disturbances (%) at mid- and subauroral latitudes (c). The TEC is a 3° latitudinal bin average over Millstone Hill longitudes (70-80°W), with non-disturbance background subtracted using the monthly average based North America TEC model [NATEC, Chen et al., 2015]. The dashed line is the approximate time of the poleward wind surge.
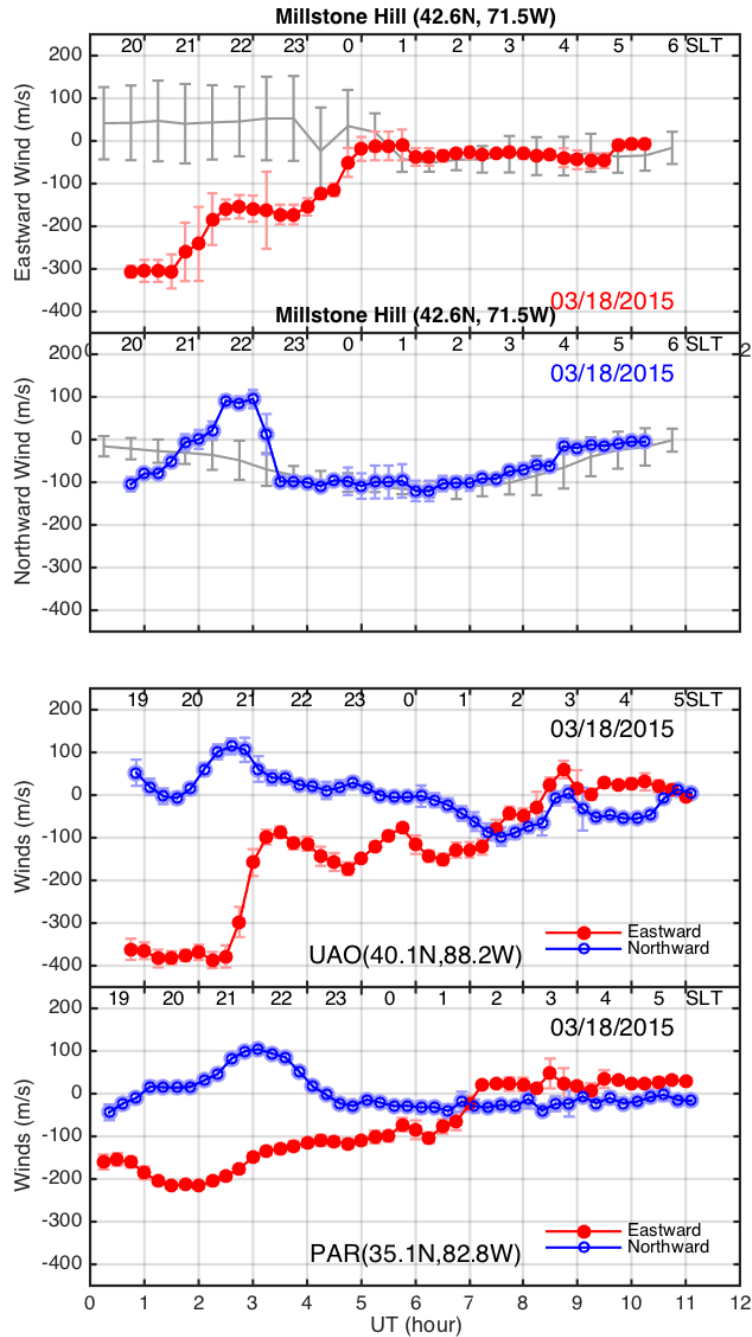
Figure 2. FPI redline neutral winds measured over Millstone Hill (top two panels, gray lines being monthly average and corresponding standard deviation; red and blue curves are winds for 18 March); over UAO and PAR (bottom two panels).

19
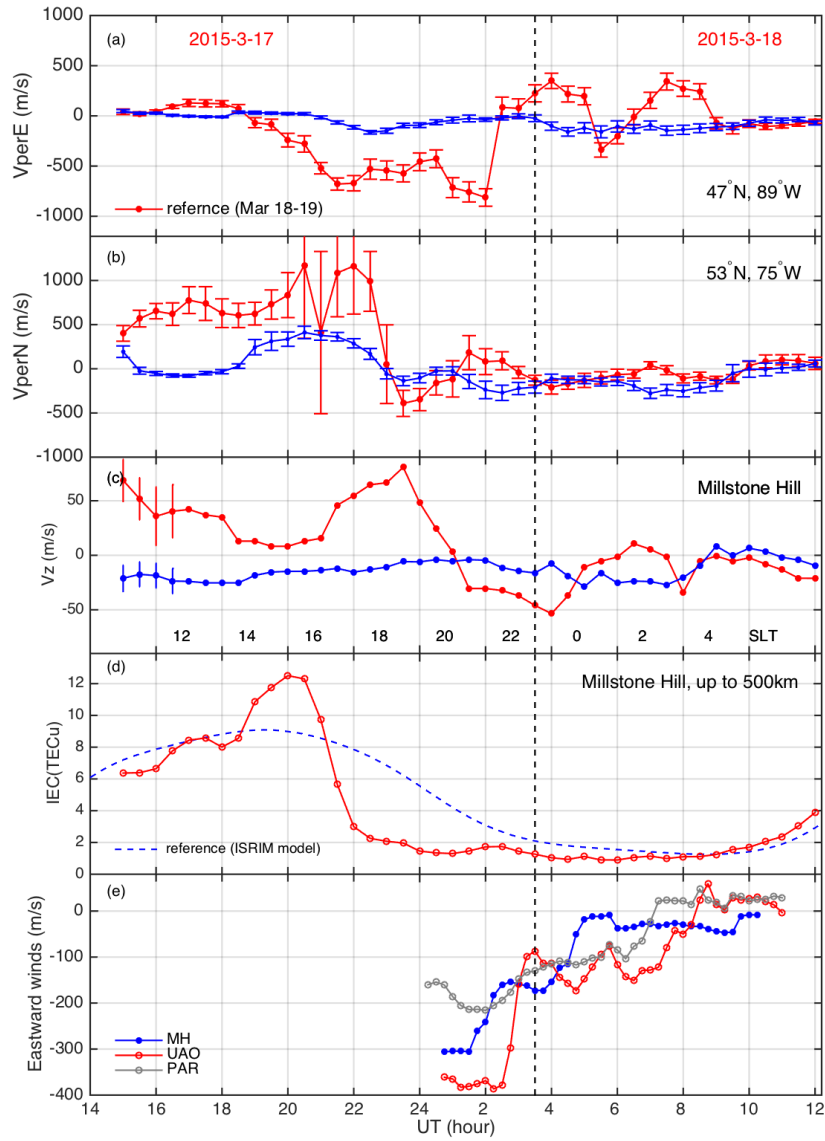
Figure 3. Millstone Hill ISR measurements of plasma drifts VperE (perpendicular east, a) for

~(89°W,47°N), VperN (perpendicular north, b) for ~(75°W, 53°N), vertical upward ion drift Vz at

250 km above MH (c), and integrated ionospheric content IEC (up to 500 km, d). Eastward winds

from Figure 2 are also given in (d). The red curves in (a)-(d) are for 17-18 March, and the blue

ones in (a) - (c) show reference drift patterns from 18-19 March observations. The dashed blue

curve in (d) is a quiet-time reference IEC variation calculated using the ISR empirical ionospheric

model ISRIM [Zhang et al., 2007a]. The vertical dashed line indicates the approximate peak time

of poleward wind surge.

552
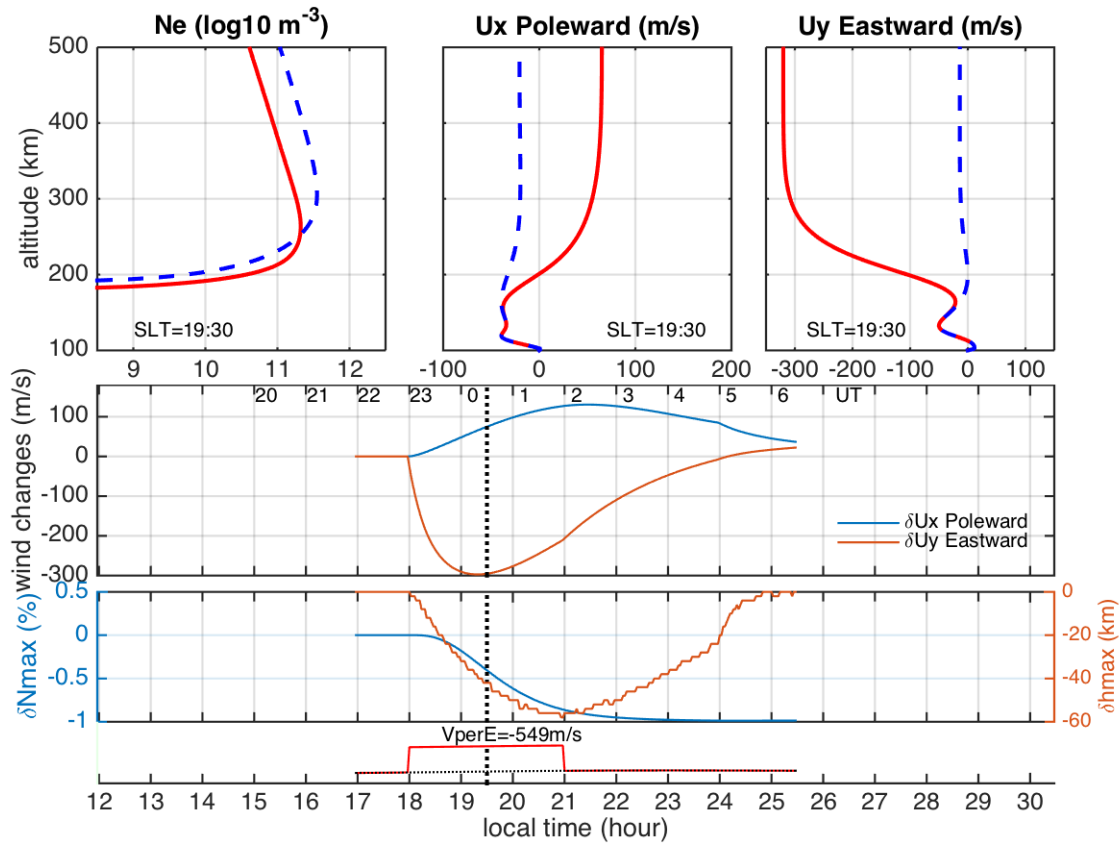
Figure 4. A numerical experiment demonstrates the mechanism of westward ion drift inducing poleward neutral winds over Millstone Hill. A westward ion drift of 500 m/s is applied over 18-20 LT (23-01UT). Profiles on the top panels show results with (red) and without (blue dashed) the strong westward ion drift at 1930 UT for electron density, poleward winds and eastward winds. The middle panel shows corresponding changes in poleward and eastward winds due to inclusion of the strong westward ion drift. The third panel plots simulated changes in the peak electron density (blue) and the peak density height (red). The bottom shows the timing of the injected 500 m/s westward ion drift.

21